The Astrophysical Journal, 760:69 (13pp), 2012 November 20 doi:10.1088/0004-637X/760/1/69

HERSCHEL PACS AND SPIRE OBSERVATIONS OF BLAZAR PKS 1510−089: A CASE FOR TWO BLAZAR ZONES

Krzysztof Nalewajko[1], Marek Sikora[2], Greg M. Madejski[3], Katrina Exter[4], Anna Szostek[3,5], Ryszard Szczerba[6], Mark R. Kidger[7], and Rosario Lorente[7]
[1] University of Colorado, UCB 440, Boulder, CO 80309, USA; knalew@colorado.edu
[2] Nicolaus Copernicus Astronomical Center, Bartycka 18, 00-716 Warsaw, Poland
[3] Kavli Institute for Particle Astrophysics and Cosmology, SLAC National Accelerator Laboratory, Stanford University, 2575 Sand Hill Road M/S 29, Menlo Park, CA 94025, USA
[4] Instituut voor Sterrenkunde, KU Leuven, Celestijnenlaan 200 D, B-3001 Leuven, Belgium
[5] Astronomical Observatory, Jagiellonian University, 30-244 Kraków, Poland
[6] Nicolaus Copernicus Astronomical Center, Rabiańska 8, 87-100, Toruń, Poland
[7] Herschel Science Centre, ESAC, P.O. Box 78, E-28691 Villanueva de la Cañada, Madrid, Spain
Received 2012 August 29; accepted 2012 October 9; published 2012 November 6

ABSTRACT

We present the results of observations of blazar PKS 1510−089 with the *Herschel Space Observatory* PACS and SPIRE instruments, together with multiwavelength data from *Fermi*/LAT, *Swift*, SMARTS, and Submillimeter Array. The source was found in a quiet state, and its far-infrared spectrum is consistent with a power law with a spectral index of $\alpha \simeq 0.7$. Our *Herschel* observations were preceded by two "orphan" gamma-ray flares. The near-infrared data reveal the high-energy cutoff in the main synchrotron component, which cannot be associated with the main gamma-ray component in a one-zone leptonic model. This is because in such a model the luminosity ratio of the external-Compton (EC) and synchrotron components is tightly related to the frequency ratio of these components, and in this particular case an unrealistically high energy density of the external radiation would be implied. Therefore, we consider a well-constrained two-zone blazar model to interpret the entire data set. In this framework, the observed infrared emission is associated with the synchrotron component produced in the hot-dust region at the supra-parsec scale, while the gamma-ray emission is associated with the EC component produced in the broad-line region at the sub-parsec scale. In addition, the optical/UV emission is associated with the accretion disk thermal emission, with the accretion disk corona likely contributing to the X-ray emission.

Key words: galaxies: active – galaxies: jets – gamma rays: galaxies – infrared: galaxies – quasars: individual (PKS 1510−089) – radiation mechanisms: non-thermal

Online-only material: color figures

1. INTRODUCTION

Of the many classes of active galactic nuclei (AGNs), blazars offer the most direct insight into the extreme plasma physics of powerful relativistic jets. The spectra of blazars span the entire range of electromagnetic radiation accessible to observational techniques and are routinely observed in the radio, millimeter, near-infrared (NIR), optical, UV, X-ray, and gamma-ray bands. Even with this enormous observational scope, we still lack a consistent theoretical picture of the dissipation and radiative processes responsible for this mostly non-thermal and strongly variable emission.

The far-infrared (FIR) window to the universe is rarely accessible owing to scarce availability of suitable observatories. Clegg et al. (1983) combined data from the Kuiper Airborne Observatory at 107 μm and 240 μm, and 400 μm data from the UKIRT telescope, with other NIR, millimeter and radio observations to construct the full infrared spectral energy distribution (SED) of blazar 3C 273. Their observations can be modeled remarkably well with a single synchrotron component. Many blazars were observed by the *Infrared Astronomical Satellite* (e.g., Impey & Neugebauer 1988) between 12 μm and 100 μm. The interpretation of their infrared spectra as synchrotron emission was strengthened by the detection of significant variability in these sources. Haas et al. (1998) observed some blazars with the *Infrared Space Observatory* between 5 μm and 200 μm. Three of the blazars had spectra consistent with a single synchrotron component, while in 3C 279 a thermal component was tentatively detected. Ogle et al. (2011) observed another prominent blazar, 3C 454.3, with the *Spitzer Space Telescope*, using all three instruments—IRS, IRAC, and MIPS. They found hints of complex structure in the spectral range of MIPS (24 μm–160 μm), which they interpreted as possible evidence for two independent synchrotron components. Another interesting result involving the *Spitzer* data was reported by Hayashida et al. (2012). They detected a sharp spectral break in blazar 3C 279 in the MIPS spectral range, with a very hard spectral index of $\alpha = 0.35 \pm 0.23$ ($F_\nu \propto \nu^{-\alpha}$) between 70 μm and 160 μm. Combined with the overall spectral shape and multiwavelength variability characteristics, this finding was also interpreted in terms of two distinct synchrotron components.

The structure of the synchrotron spectral component in blazars is of great importance for understanding the physical structure of the so-called "blazar zone" in relativistic AGN jets. It became clear that more detailed FIR observations of blazars are needed. A great opportunity came with the launch of the *Herschel Space Observatory*. In this work, we present photometric observations of another prominent blazar, PKS 1510−089, with two *Herschel* instruments—PACS and SPIRE. These results are combined with the publicly available multiwavelength data from *Fermi*/LAT, *Swift*, SMARTS, and the Submillimeter Array (SMA). PKS 1510−089 was observed previously by Malmrose et al. (2011) in the mid-IR (MIR) band with *Spitzer* (IRS, IRAC, and MIPS), who looked for signatures of thermal emission from the dusty torus but found the source spectrum to be consistent with a power law. It is also a prominent

Table 1
The *Herschel* Observing Log for PKS 1510−089

Epoch	MJD	PACS					SPIRE
		Filter	OID		Speed		OID
			s	xs	s	xs	
H1	55774	r+b	24997	24998	m	f	24992
	···	r+g	25102	25103	f	f	
H2	55790	r+b	26661	26662	m	f	26659
	···	r+g	26709	26710	f	f	
H3	55794	r+b	27007	27008	f	m	27002
	···	r+g	27041	27042	f	f	
H4	55806−55807	r+b	27805	27806	f	m	27048
	···	r+g	27833	27834	f	f	
H5	55813−55814	r+b	28361	28362	f	m	28355
	···	r+g	28393	28394	f	f	

Notes. Individual observations have unique identifiers (OID). For each observational epoch (first column), we performed four scanning-mode observations with PACS (s: scan; xs: cross-scan), each with a combination of two filters out of three (r: red; g: green; b: blue) and one of two scanning speeds (m: medium; f: fast); as well as one small-map observation with SPIRE.

gamma-ray source. In the spring of 2009, it showed a series of strong gamma-ray flares that were probed by *Fermi*/LAT (Abdo et al. 2010a) and *AGILE* (D'Ammando et al. 2011). During this time, it was also detected at very high energies (∼0.1–1 TeV) by the H.E.S.S. observatory (Wagner & Behera 2010) as one of a handful of FSRQs known at these energies.

In Section 2, we report on our *Herschel* observations and other multiwavelength data. In Section 3, we present the observational results, in particular multiwavelength light curves and quasi-simultaneous SEDs. In Section 4, we present our model of the broadband SED of PKS 1510−089. In Section 5, we discuss how our results compare to previous studies of PKS 1510−089. Our conclusions are given in Section 6.

In this work, symbols with a numerical subscript should be read as a dimensionless number $X_{\rm n} = X/(10^n$ cgs units). We adopt a standard ΛCDM cosmology with $H_0 = 71\,{\rm km\,s^{-1}\,Mpc^{-1}}$, $\Omega_{\rm m} = 0.27$, and $\Omega_\Lambda = 0.73$, in which the luminosity distance to PKS 1510−089 ($z = 0.36$) is $d_{\rm L} = 1.91$ Gpc.

2. OBSERVATIONS

2.1. Herschel

We observed PKS 1510−089 with the *Herschel Space Observatory* (Pilbratt et al. 2010), using the PACS (Poglitsch et al. 2010) and SPIRE (Griffin et al. 2010) instruments, in five epochs denoted as "H1"–"H5" between 2011 August 1 (MJD 55774) and 2011 September 10 (MJD 55814)—see Table 1. The PACS and SPIRE observations for each epoch took place no more than one-day apart.

2.1.1. Data Reduction

The PACS observations[8] are mini-scan maps taken in pairs with scan and cross-scan positional angles of 70° and 110°, respectively, and with 10 scan legs, each of 3.′5 length and 2″ separation. For each epoch, the PACS observations were repeated to cover the blue+red and the green+red bands. The characteristic wavelengths for the red, green, and blue bands are 160 μm, 100 μm, and 70 μm, respectively. Both medium and fast scan speeds were used. The SPIRE observations[9] used the standard small-scan map method, and each observation returned fluxes in three bands: short (PSW (photometer short wavelength); 250 μm), medium (PMW (photometer medium wavelength); 350 μm), and long (PLW (photometer long wavelength); 500 μm). The details are recorded in Table 1, including the date, observation ID, and (for PACS) the filter and scan speed.

The PACS observations were reduced using HIPE, a *Herschel*-specific software package (Ott 2010). We used the `Track 9` pipeline starting from `Level 0`, and with the calibration tree `v32`. The pipeline tasks included crosstalk correction, nonlinearity correction, and second-level de-glitching (`mapDeglitch` task with the `timeordered` option on). The background was removed using the high-pass filter method, adopting filter widths of 15, 20, and 35 readouts for blue, green, and red bands, respectively; source masking radius of 25″ for all bands; and drop size (`pixfrac`) of 1. The map pixel sizes are 1.″1, 1.″4, and 2.″1 for the blue, green, and red bands, respectively.

The SPIRE observations were also reduced using the HIPE, with the `Track 9` pipeline starting from `Level 0.5`, and with the calibration version `spire_cal_1`. To remove the background, we used the `destriping` task with standard parameter settings. The maps were made with pixel sizes of 6″, 10″, and 14″ for the PSW, PMW, and PLW bands, respectively. Background sources were fitted and removed with the source extractor routine (removing only those that appeared at all epochs). The SPIRE maps were converted to units of Jy pixel^{-1}, to match the units of the PACS maps, using the recommended beam-to-pixel size conversion factors.

2.1.2. Photometry

All maps were measured for photometric fluxes using the aperture photometry with recommended aperture sizes for the source and the sky, and published aperture corrections.[10] For SPIRE, we obtained two additional flux measurements by fitting the source `on the map` (a standard HIPE task) and `along the timeline`.[11] The final adopted flux value is the mean of the three measurements, with the differences between results for each epoch never exceeding 0.01 Jy (<2%). The calibration uncertainties are reported to be 5% for PACS and 7% for SPIRE. No color corrections were applied to the measured fluxes, the SPIRE and PACS calibration assume a source spectral index of $\alpha = 1$ ($F_\nu \propto \nu^{-\alpha}$).

In all six bands, we checked whether PKS 1510−089 is a point source. We computed the radial flux profiles by measuring the flux in apertures of increasing radius, and compared them to the flux profiles produced from the point-spread function (PSF) maps for each instrument (PACS: from FITS files provided on the instrument public page; SPIRE: from a calibration file). In all cases, the blazar was compatible with a point source.

For the PACS maps, we had a mixture of the fast and medium scan speeds: observations in the green band were taken with the fast scan speeds only, and those in the blue and red bands were taken with either of the two scan speeds. The available aperture corrections have been produced only for the medium (and slow)

[8] The PACS Observer's Manual is available at http://herschel.esac.esa.int/Docs/PACS/html/pacs_om.html

[9] The SPIRE Observer's Manual is available at http://herschel.esac.esa.int/Docs/SPIRE/html/spire_om.html

[10] "PACS instrument and calibration"—http://herschel.esac.esa.int/twiki/bin/view/Public/PacsCalibrationWeb; "SPIRE instrument and calibration"—http://herschel.esac.esa.int/twiki/bin/view/Public/SpireCalibrationWeb

[11] We used a script provided by the SPIRE team: `bendoSourceFit_v9.py`.

Table 2
Photometric Results of the *Herschel* PACS and SPIRE Observations of PKS 1510−089

	PACS			SPIRE		
	Blue (70 μ)	Green (100 μm)	Red (160 μm)	PSW (250 μm)	PMW (350 μm)	PLW (500 μm)
H1 (MJD 55774)	0.52 ± 0.01	0.36 ± 0.02	0.29 ± 0.02	0.67 ± 0.02	0.83 ± 0.02	0.99 ± 0.01
H2 (MJD 55790)	0.46 ± 0.01	0.33 ± 0.02	0.22 ± 0.02	0.61 ± 0.02	0.79 ± 0.02	0.96 ± 0.01
H3 (MJD 55794)	0.48 ± 0.01	0.35 ± 0.02	0.25 ± 0.02	0.64 ± 0.02	0.84 ± 0.02	1.02 ± 0.01
H4 (MJD 55806−55807)	0.39 ± 0.01	0.28 ± 0.02	0.20 ± 0.02	0.55 ± 0.02	0.72 ± 0.02	0.92 ± 0.01
H5 (MJD 55813−55814)	0.38 ± 0.01	0.31 ± 0.02	0.22 ± 0.02	0.57 ± 0.02	0.74 ± 0.02	0.93 ± 0.01

Note. The fluxes are given in units of Jy.

scan speeds, hence for the fast scan speeds there is an additional uncertainty of a few percent in the flux measurement (based on a comparison of their PSFs: PACS team communication). In addition, the signal-to-noise ratio is slightly worse on the fast scan speed maps. Therefore, we used only the medium scan speed map fluxes for the red and blue bands, and the average of the fast scan speed map fluxes for the green band. To check on the difference in photometry between scan speeds, we compared the results for fast and medium scan speed maps in the red and green: the difference is not greater than 0.02 Jy for both bands. This value is similar to the typical flux measurement errors (see Table 2).

For all maps, we measure the scatter in the background as the standard deviation between about eight apertures placed in background regions, which currently is the best method of estimating the flux measurement uncertainty. Since the background is devoid of any obvious traces of the interstellar medium, the observing mode is the same for all the epochs, and the data are reduced in the same way, we report only one average flux error for each of the six bands covered by PACS and SPIRE. The final results of the PACS and SPIRE photometry of PKS 1510−089 are reported in Table 2.

2.2. *Fermi*/LAT

The *Fermi*/LAT telescope (Atwood et al. 2009) for most of 2011 operated in the scanning mode, observing the entire sky frequently and fairly uniformly. We used the standard analysis software package `Science Tools v9r27p1`, with the instrument response functions `P7SOURCE_V6` (*Fermi*-LAT Collaboration 2012), the Galactic diffuse emission model `gal_2yearp7v6_v0`, and the isotropic background model `iso_p7v6source`. Events of the `SOURCE` class were extracted from the region of interest (ROI) of 10° radius centered on the position of PKS 1510−089 ($\alpha = 228.^{\circ}2$, $\delta = -9.^{\circ}1$). The background model included 17 sources from the *Fermi*/LAT Second Source Catalog (Nolan et al. 2012) within 15° from PKS 1510−089; their spectral models are power laws with the photon index fixed to the catalog values, and for sources outside the ROI the normalizations were also fixed. In addition, our source model included TXS 1530−131, located 6° from PKS 1510−089, which was in a flaring state (Gasparrini & Cutini 2011). The free parameters of the source model are the normalizations of all point sources within the ROI, as well as of the diffuse components, and the photon indices of PKS 1510−089 and TXS 1530−131. The source flux was calculated with the unbinned maximum likelihood method, following standard recommendations[12] (zenith angle <100° and the `gtmktime` filter `(DATA_QUAL==1) && (LAT_CONFIG==1) && ABS(ROCK_ANGLE)<52`). Measurements with the test statistic TS $\geqslant$ 10 (Mattox et al. 1996) and with the predicted number of gamma rays $N_{\rm pred} \geqslant 3$ are presented in figures as data points. For the SEDs, we also plot 2σ upper limits calculated with a method described in Section 4.4 of Abdo et al. (2010c).

To calculate the medium-term light curve, we selected events registered between MJD 55740 and MJD 55830 of reconstructed energy between $E_{\rm min} = 200$ MeV and $E_{\rm max} = 300$ GeV. The spectrum of PKS 1510−089 was modeled with a power law with a free photon index. The light curve is presented with overlapping three-day bins with a one-day time step. The νF_ν values are calculated from the fitted power-law model at photon energies of 200 MeV and 2 GeV.

To calculate the long-term light curve, we selected events between MJD 54700 and MJD 55840, and modeled them in six-day bins. We used the same energy range as before, and the νF_ν values correspond to the photon energy of 2 GeV.

To calculate the SEDs, we selected events registered over three-day time intervals (MJD 55789−55792 for the "H2" state, MJD 55766−55769 for the "F2" state; see below) in overlapping energy bins of equal logarithmic width and uniform logarithmic spacing:

$$E_{\rm min}\left(\frac{E_{\rm max}}{E_{\rm min}}\right)^{(i-k)/N} \leqslant E \leqslant E_{\rm min}\left(\frac{E_{\rm max}}{E_{\rm min}}\right)^{i/N} \quad (1)$$

with $E_{\rm min} = 100$ MeV, $E_{\rm max} = 100$ GeV, $k = 3$, $N = 18$, and $i \in \{k, \ldots, N\}$. Within each bin, the spectrum of PKS 1510−089 was modeled with a power law with a fixed photon index determined from power-law fits in the broad energy range 200 MeV $\leqslant E \leqslant$ 300 GeV: $\Gamma_{\rm H2} = 2.44$ and $\Gamma_{\rm F2} = 2.30$.

2.3. *Swift*

2.3.1. XRT Data Analysis

We analyzed the *Swift*/XRT data following the recommendations given in the "Data Reduction Guide v1.2." We used the `ftools` software package v6.11, the *Swift* calibration files from 2011 November, and the `xspec` program v12.7.0. We started from Level 1 event files, and reduced the data using the `xrtpipeline` script with default screening and filtering criteria. With `xrtpipeline`, we created the exposure maps and used them to correct the `arf` files for dead columns. We extracted the source and the background spectra, using the `xselect` program v2.4b, from a circular region centered on the source and with a radius of 47″. The background came from an annulus centered on the source and with inner and outer radii of 80″ and 135″, respectively. To obtain the spectral parameters, we fitted observations which have more than 75 source counts with an absorbed power-law model with hydrogen column density fixed

[12] http://fermi.gsfc.nasa.gov/ssc/data/analysis/documentation/Cicerone/

Table 3
Fit Results for the *Swift*/XRT Observations of PKS 1510−089

Obs ID	Date MJD	Exposure (s)	Counts src	Counts bkg	0.3–10 keV Flux (10^{-12} erg cm^{-2} s^{-1})	Γ_X	Norm (10^{-3} keV^{-1} cm^{-2} s^{-1})	Reduced χ^2
31173075	55735.20	1301.29	140	4	$7.42^{+1.58}_{-1.00}$	$1.68^{+0.17}_{-0.17}$	$1.05^{+0.14}_{-0.13}$	0.49
31173076	55742.08	1010.44	100	3	$7.34^{+2.82}_{-1.59}$	$1.48^{+0.33}_{-0.31}$	$0.86^{+0.17}_{-0.16}$	2.26
31173077	55746.87	2828.23	391	38	$8.38^{+1.04}_{-0.88}$	$1.40^{+0.09}_{-0.09}$	$0.90^{+0.07}_{-0.07}$	0.91
31173078	55749.32	3853.72	535	6	$8.16^{+0.82}_{-0.71}$	$1.53^{+0.08}_{-0.08}$	$1.01^{+0.06}_{-0.06}$	1.47
31173079	55758.13	288.34	20	1	...	...	...	...
31173080	55760.18	1913.07	284	3	$10.00^{+1.69}_{-1.40}$	$1.52^{+0.13}_{-0.13}$	$1.22^{+0.10}_{-0.11}$	0.41
31173081	55762.48	1667.35	224	5	$9.20^{+1.80}_{-1.48}$	$1.39^{+0.14}_{-0.13}$	$0.98^{+0.10}_{-0.10}$	0.81
31173082	55766.68	1995.81	350	16	$10.18^{+1.69}_{-1.20}$	$1.52^{+0.11}_{-0.10}$	$1.23^{+0.09}_{-0.09}$	1.73
31173083	55768.47	2166.31	370	9	$9.68^{+1.22}_{-1.01}$	$1.60^{+0.10}_{-0.10}$	$1.27^{+0.09}_{-0.09}$	0.98
31173084	55770.51	1709.98	305	13	$10.61^{+1.42}_{-1.19}$	$1.54^{+0.11}_{-0.11}$	$1.32^{+0.11}_{-0.11}$	0.80
31173085	55772.22	1898.03	291	4	$9.99^{+1.45}_{-1.26}$	$1.39^{+0.11}_{-0.11}$	$1.05^{+0.10}_{-0.10}$	0.86
31173086	55774.19	2023.39	330	5	$10.04^{+1.50}_{-1.09}$	$1.58^{+0.11}_{-0.11}$	$1.30^{+0.11}_{-0.11}$	0.78
31173087	55776.33	388.63	40	0	...	...	...	...
31173088	55778.14	1702.46	202	5	$7.31^{+1.12}_{-0.99}$	$1.63^{+0.14}_{-0.14}$	$0.99^{+0.10}_{-0.10}$	0.47
31173089	55782.58	1664.85	283	4	$10.42^{+1.26}_{-1.17}$	$1.65^{+0.12}_{-0.12}$	$1.43^{+0.13}_{-0.13}$	0.70
31173090	55784.67	1777.68	349	4	$12.88^{+1.80}_{-1.41}$	$1.46^{+0.10}_{-0.10}$	$1.47^{+0.12}_{-0.12}$	0.57
31173091	55786.51	2401.99	407	6	$11.79^{+1.54}_{-1.34}$	$1.30^{+0.09}_{-0.09}$	$1.12^{+0.08}_{-0.08}$	0.90
31173092	55788.89	2474.71	363	5	$9.93^{+1.41}_{-1.21}$	$1.29^{+0.10}_{-0.10}$	$0.93^{+0.08}_{-0.08}$	0.97
31173093	55790.49	2045.96	346	27	$10.85^{+1.63}_{-1.22}$	$1.39^{+0.11}_{-0.11}$	$1.14^{+0.10}_{-0.10}$	1.03
31173094	55793.66	1130.79	181	8	$12.38^{+3.42}_{-2.44}$	$1.31^{+0.17}_{-0.17}$	$1.19^{+0.14}_{-0.14}$	1.28
31173095	55796.19	2048.46	350	6	$12.61^{+1.64}_{-1.57}$	$1.27^{+0.10}_{-0.10}$	$1.17^{+0.10}_{-0.10}$	0.98
31173096	55799.65	2033.42	284	5	$9.88^{+1.68}_{-1.32}$	$1.25^{+0.11}_{-0.11}$	$0.89^{+0.08}_{-0.08}$	1.18

Notes. The spectrum was fitted in the 0.3–10 keV band with a model `wabs*powerlaw`, the hydrogen column density N_H was fixed at 7.9×10^{20} cm^{-2}, and the free photon index Γ_X. The reported flux values correspond to the de-absorbed spectrum. Errors on the normalization parameter and Γ_X are 1σ. Flux errors correspond to 90% confidence interval using xspec script `fluxerror.tcl`. Background counts are scaled to the size of the source region using `backscal` keyword. Observations with less than 75 counts were not fitted.

at its Galactic value of 7.9×10^{20} cm^{-2} (Kataoka et al. 2008), and with a free photon index. To calculate the flux errors, we used the script `fluxerror.tcl` provided by the `xspec` team.[13] The results are given in Table 3.

2.3.2. UVOT Data Analysis

To analyze the UVOT data in the image mode, we followed the recommendations from the "UVOT Software Guide v2.2," and started from the Level 1 raw data. We constructed a bad pixel map for each exposure to remove the bad pixels from further analysis. We reduced a `modulo8` fixed-pattern noise from the images and the pixel-to-pixel fluctuations in the images due to detector sensitivity variations. Then, we converted the images from a raw coordinate system to a tangential projection on the sky. Before adding the images, we applied an aspect-ratio correction to each exposure to obtain the correct sky coordinates of the UVOT sources and to ensure that individual exposures were added without offsets. Finally, we added all image exposures for a specific filter in a given observation. To extract the source magnitude and counts, we used the `uvotsource` task. We used an aperture of 5″ for all filters, which matches the aperture used to calibrate the UVOT photometry, and therefore it does not require aperture corrections. The background is estimated from an annulus with radii of 15″ and 25″ centered on the source. The results are presented in Table 4.

To convert the observed magnitudes m_λ to flux densities νF_ν, we introduce an effective zero point Z_λ, such that $\nu F_\nu(\mathrm{erg\,s^{-1}\,cm^{-2}}) = 10^{(Z_\lambda - m_\lambda + A_\lambda)/2.5}$, where A_λ is the extinction. For *Swift*/UVOT, we took

$$Z_\lambda^{(\mathrm{UVOT})} = Z_\lambda^{(\mathrm{P08})} + 2.5 \log \left(\lambda_{\mathrm{eff}}^{(\mathrm{P08})}(\text{Å}) \times C_{\mathrm{F}}^{(\mathrm{P08})}(\mathrm{erg\,s^{-1}\,cm^{-2}\,Å^{-1}})\right), \quad (2)$$

where $Z_\lambda^{(\mathrm{P08})}$, $\lambda_{\mathrm{eff}}^{(\mathrm{P08})}$, and $C_{\mathrm{F}}^{(\mathrm{P08})}$ are parameters taken from Tables 6, 8, and 10 in Poole et al. (2008), respectively. We adopt $\lambda_{\mathrm{eff}}^{(\mathrm{P08})}$ as the effective wavelength for the UVOT filters. For the extinction correction in the direction to PKS 1510−089, we adopted a standard Galactic extinction model by Cardelli et al. (1989) with parameters $E(B-V) = 0.101$ and $R_V = 3.1$. In Table 5, we report the effective wavelengths, extinctions, and effective zero points for UVOT filters U, $W1$, $M2$, and $W2$. The effective zero points for filters V and B are consistent with the Cousins–Glass–Johnson photometric system discussed in Section 2.4.

2.4. SMARTS and SMA

We used public optical and NIR data (B, V, R, J, and K filters) from the Yale University SMARTS project.[14] A part of the data for PKS 1510−089 was presented in Bonning et al. (2012).

[13] http://heasarc.nasa.gov/xanadu/xspec/fluxerror.html

[14] http://www.astro.yale.edu/smarts/glast/

Table 4
The Results of *Swift*/UVOT Photometry for PKS 1510−089

Obs ID	Date	*V*	*B*	*U*	*W1*	*M2*	*W2*
00031173075	55735.19	4.65 ± 0.38	6.69 ± 0.30	6.99 ± 0.30	6.01 ± 0.32	7.92 ± 0.37	6.71 ± 0.27
00031173076	55742.08	5.03 ± 0.44	7.63 ± 0.36	8.32 ± 0.36	7.21 ± 0.39	9.77 ± 0.45	9.47 ± 0.37
00031173077	55746.78	6.24 ± 0.49	7.80 ± 0.23	8.49 ± 0.25	7.38 ± 0.29	10.12 ± 0.18	9.65 ± 0.28
00031173078	55749.18	6.85 ± 0.26	8.54 ± 0.20	9.24 ± 0.23	7.83 ± 0.30	10.63 ± 0.25	10.09 ± 0.27
00031173079	55758.13	...	...	8.95 ± 0.59	6.83 ± 0.33	...	...
00031173080	55760.14	5.15 ± 0.32	7.22 ± 0.26	7.72 ± 0.27	6.65 ± 0.30	8.72 ± 0.34	8.38 ± 0.27
00031173081	55762.34	6.67 ± 0.39	7.88 ± 0.32	8.38 ± 0.31	7.66 ± 0.35	10.15 ± 0.37	9.50 ± 0.31
00031173082	55766.64	7.71 ± 0.38	9.05 ± 0.28	9.55 ± 0.30	7.88 ± 0.34	10.75 ± 0.35	9.39 ± 0.30
00031173083	55768.43	6.56 ± 0.34	8.13 ± 0.27	8.86 ± 0.28	7.70 ± 0.33	8.90 ± 0.43	9.64 ± 0.29
00031173084	55770.38	6.39 ± 0.35	8.07 ± 0.27	8.88 ± 0.29	7.97 ± 0.34	10.41 ± 0.33	8.98 ± 0.29
00031173085	55772.13	5.28 ± 0.34	6.99 ± 0.27	7.78 ± 0.28	6.44 ± 0.30	9.66 ± 0.34	8.76 ± 0.29
00031173086	55774.12	7.58 ± 0.37	8.92 ± 0.29	9.02 ± 0.29	7.81 ± 0.34	10.04 ± 0.34	9.25 ± 0.29
00031173087	55776.47	...	6.83 ± 0.38	8.10 ± 0.38	6.61 ± 0.34	...	11.67 ± 1.36
00031173088	55778.06	5.33 ± 0.38	6.84 ± 0.30	7.11 ± 0.28	6.19 ± 0.31	9.24 ± 0.32	8.54 ± 0.30
00031173089	55782.48	5.91 ± 0.40	7.83 ± 0.31	8.26 ± 0.31	7.11 ± 0.34	9.84 ± 0.37	9.44 ± 0.32
00031173090	55784.57	7.36 ± 0.62	9.49 ± 0.28	10.31 ± 0.30	8.94 ± 0.37	12.30 ± 0.57	11.27 ± 0.33
00031173091	55786.31	8.86 ± 0.37	10.79 ± 0.28	11.49 ± 0.31	10.44 ± 0.41	12.31 ± 0.35	11.35 ± 0.33
00031173092	55788.78	5.95 ± 0.32	6.89 ± 0.24	7.86 ± 0.25	6.96 ± 0.30	9.47 ± 0.29	9.41 ± 0.28
00031173093	55790.19	6.75 ± 0.35	8.34 ± 0.27	8.90 ± 0.28	7.55 ± 0.32	10.73 ± 0.33	10.22 ± 0.31
00031173094	55793.66	3.78 ± 0.40	6.88 ± 0.33	7.72 ± 0.32	6.96 ± 0.36	8.80 ± 0.54	9.07 ± 0.33
00031173095	55796.06	5.43 ± 0.35	6.77 ± 0.30	7.77 ± 0.28	6.76 ± 0.31	9.08 ± 0.33	8.74 ± 0.28
00031173096	55799.61	4.57 ± 0.33	6.19 ± 0.26	7.37 ± 0.26	6.07 ± 0.28	8.85 ± 0.33	8.41 ± 0.27

Notes. We report flux densities νF_ν corrected for extinction, in units of 10^{-12} erg s^{-1} cm^{-2}. Quoted errors are a sum of 1σ statistical and a systematic error added in quadrature. Systematic errors are of the order of 5%.

Table 5
Effective Wavelengths, Extinctions and Effective Zero Points for the SMARTS ($K-B$) and *Swift*/UVOT ($U-W2$) Filters

Filter	$\lambda_{\rm eff}$ (μm)	A_λ (mag)	$Z_{\lambda,\rm eff}$
K	2.19	0.04	−15.14
J	1.22	0.09	−13.52
R	0.641	0.26	−12.11
V	0.545	0.32	−11.75
B	0.438	0.42	−11.39
U	0.350	0.50	−12.27
W1	0.263	0.66	−12.45
M2	0.223	0.96	−12.49
W2	0.203	0.92	−12.40

The magnitudes m_λ were converted into flux densities using the effective zero points introduced in Section 2.3.2, here calculated as

$$Z_\lambda^{(\rm SMARTS)} = 2.5\log(\nu_{\rm eff}({\rm Hz}) \times f_\nu^{(\rm B98)}({\rm erg\,s^{-1}\,cm^{-2}\,Hz^{-1}}))\,, \quad (3)$$

where $\nu_{\rm eff} = c/\lambda_{\rm eff}^{(\rm B98)}$, and $\lambda_{\rm eff}^{(\rm B98)}$ and $f_\nu^{(\rm B98)}$ are parameters of the Cousins–Glass–Johnson photometric system taken from Table A2 in Bessell et al. (1998). The effective wavelengths and zero points for each SMARTS filter are reported in Table 5.

We obtained the SMA data for PKS 1510−089 at 1.3 mm wavelength from the SMA Callibrator List[15] (Gurwell et al. 2007). We use these data only to verify that they lie on the power-law extrapolation of the *Herschel* PACS and SPIRE SED.

[15] http://sma1.sma.hawaii.edu/callist/callist.html

Table 6
Spectral Fits to the *Herschel* PACS and SPIRE Data for Each Observation Epoch

Epoch	α	$\log(\nu F_\nu$ (erg s^{-1} cm^{-2})) at 10^{12} Hz
H1	0.64 ± 0.02	−11.130 ± 0.007
H2	0.74 ± 0.04	−11.158 ± 0.019
H3	0.71 ± 0.02	−11.135 ± 0.007
H4	0.766 ± 0.012	−11.201 ± 0.004
H5	0.75 ± 0.04	−11.192 ± 0.014

Note. The model is a power-law function in the form $F_\nu \propto \nu^{-\alpha}$.

3. RESULTS

3.1. Herschel PACS and SPIRE

Figure 1 shows the light curves of PKS 1510−089 calculated for each filter of the PACS and SPIRE instruments. The source was not significantly variable over weekly timescales across the entire spectral range. The slight variations observed at different wavelengths appear to be correlated.

Figure 2 shows the FIR SEDs of PKS 1510−089 in five epochs; for each epoch observations in all six bands were performed within one day. These SEDs are generally consistent with power laws. The parameters of the spectral fits for each observational epoch are reported in Table 6. A slight harder-when-brighter trend is apparent, although the range of parameter values is rather small.

3.2. Multiwavelength Data

To provide a context for the results obtained with *Herschel*, we analyze quasi-simultaneous multiwavelength data for PKS 1510−089: gamma-ray data from *Fermi*/LAT, optical/UV and X-ray data from *Swift*, optical/NIR data from SMARTS, and millimeter data from SMA. In Figure 3, we

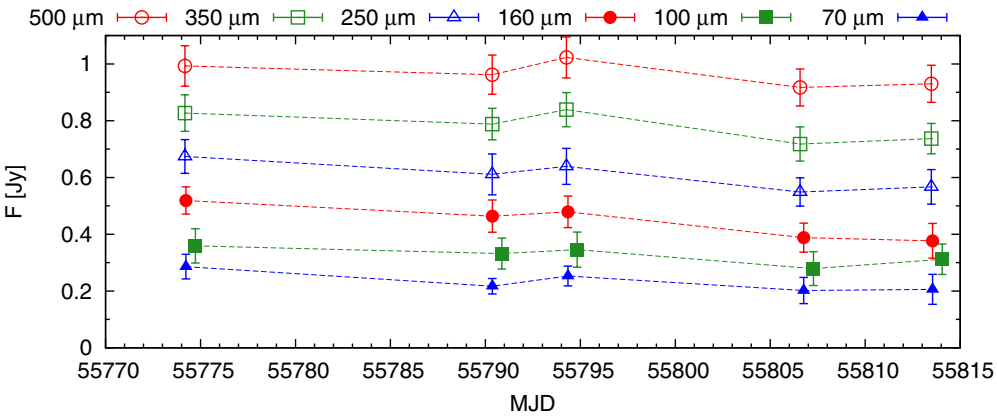

Figure 1. *Herschel* PACS (filled symbols) and SPIRE (empty symbols) light curves of PKS 1510−089.
(A color version of this figure is available in the online journal.)

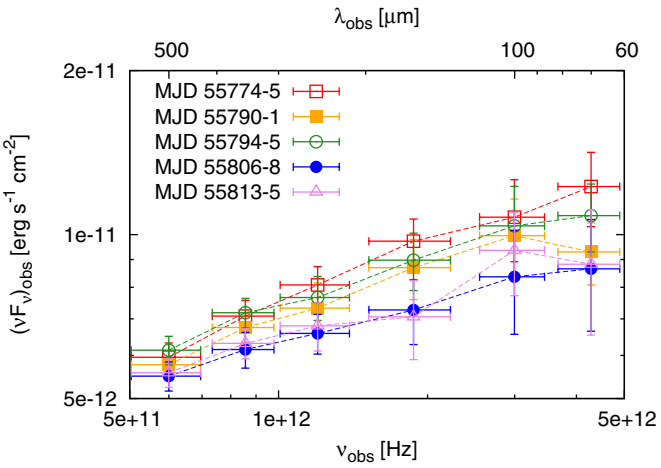

Figure 2. *Herschel* PACS and SPIRE quasi-simultaneous spectral energy distributions of PKS 1510−089.
(A color version of this figure is available in the online journal.)

present multiwavelength light curves calculated over a period of ∼3 months encompassing our *Herschel* campaign. The simultaneous multiwavelength coverage varies between different *Herschel* pointings. The *Herschel* observations span a period of relatively low activity following two prominent gamma-ray flares—"F1" (MJD 55745; D'Ammando & Gasparrini 2011) and "F2" (MJD 55767).[16] The *Fermi*/LAT data indicate a modest spectral variability across the gamma-ray band. The F2 gamma-ray flare has a possible optical/NIR counterpart seen in the SMARTS data (see also Hauser et al. 2011). The discrete correlation function (Edelson & Krolik 1988) calculated between the *Fermi*/LAT data at 2 GeV and the SMARTS data in the *V* band (Figure 4) indicates that the optical flux is delayed with respect to the gamma-ray flux by one to two days. However, such correlation is not confirmed by the *Swift*/UVOT data, the brighter F1 gamma-ray flare does not have a similar optical counterpart, and the amplitude of optical variability is one order of magnitude smaller than the amplitude of the gamma-ray flare. Thus, these two gamma-ray flares can be practically called "orphan" flares. Of the NIR/optical/UV bands, the most prominent activity is seen in the *K* band.

We extracted the broadband SEDs of PKS 1510−089 for two epochs. The second *Herschel* pointing (H2) is chosen among other *Herschel* pointings for the best overall multiwavelength coverage and the highest simultaneous gamma-ray flux. The second gamma-ray flare (F2) has a better multiwavelength coverage than the first gamma-ray flare. These two SEDs are shown in Figure 5. We find a very good agreement in the NIR/optical/UV and X-ray bands between these two epochs. There is a prominent difference in the gamma-ray band, not only in the integrated luminosity, but also in the spectral shape. In the low gamma-ray state (H2), the gamma-ray spectrum is much softer and can be reasonably approximated with a single power law. In the high gamma-ray state (F2), a possible double structure is seen, with peaks at ∼250 MeV and ∼1.5 GeV, and a dip at ∼700 MeV.[17] The spectrum in the F2 state is significantly harder, at least up to ∼3 GeV. Because of such a hard spectrum, the integrated luminosity calculated by fitting a power-law model up to 100 GeV might be significantly overestimated.

The FIR/millimeter spectrum probed by *Herschel* and SMA is consistent with a simple power law. While the highest frequency PACS point (70 μm) in the H2 state indicates a small discrepancy from this trend, the *Herschel* data at other epochs do not show any persistent spectral structure there. We note that the spectral index measured by *Herschel* is consistent with the non-simultaneous observations in overlapping spectral windows by *Planck* and *Spitzer*. Such a well-aligned power-law spectrum can be naturally explained with a single synchrotron component in the optically thin regime. An interesting question is how this component connects to the NIR/optical data. In the NIR band, the SMARTS data indicate a peculiarly soft spectrum between *K* and *J* bands, as compared to a hard optical/UV spectrum between *R* and *W*2 bands (a similar NIR spectrum can be seen in the data presented by Impey & Neugebauer 1988). Such a feature can be understood only as the high-energy end of the synchrotron component. In Section 4, we consider a model in which the FIR and NIR spectra are connected with a single synchrotron component.

3.3. Long-term Variability

In Figure 6, we compare the long-term light curves collected in the gamma-ray and optical/NIR bands by *Fermi*/LAT and

[16] Two more prominent gamma-ray flares were observed in PKS 1510−089 in 2011 October–November (Orienti et al., 2012).

[17] Whether this is a real spectral feature or just a statistical fluctuation requires a more detailed analysis. Our conclusions do not rely on this issue.

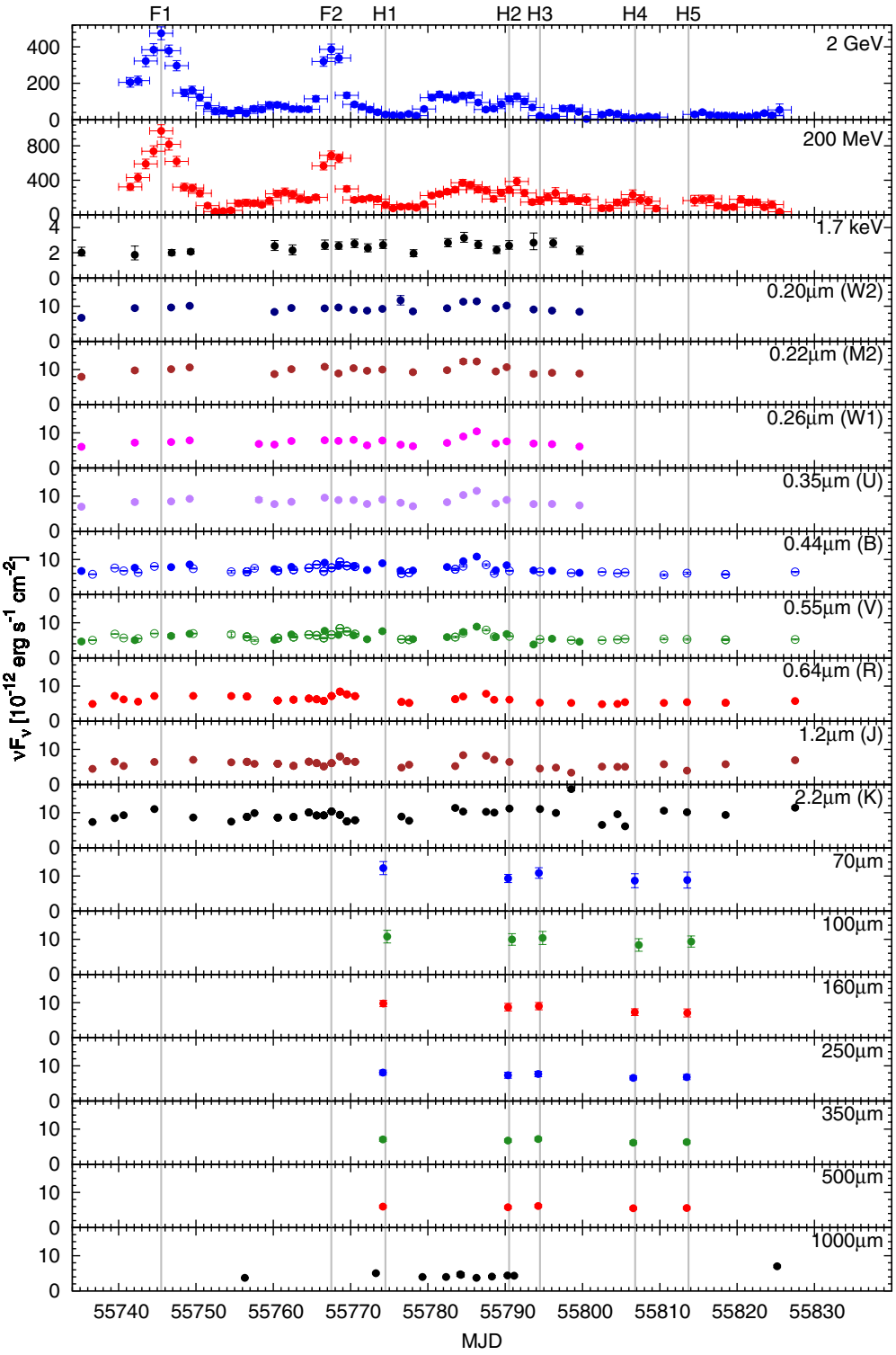

Figure 3. Multiwavelength light curves of PKS 1510−089, including data from SMA, *Herschel* PACS and SPIRE, SMARTS, *Swift* UVOT and XRT, and *Fermi*/LAT. The *Swift*/XRT and *Fermi*/LAT light curves are calculated at the indicated photon energies from power-law fits over broader energy ranges (0.3–10 keV and 0.2–300 GeV, respectively). All panels use the same units. The SMARTS and *Swift*/UVOT data are corrected for extinction. Vertical lines indicate the two *Fermi* flares ("Fn") and the five *Herschel* epochs ("Hn").

(A color version of this figure is available in the online journal.)

SMARTS, respectively. These data include a previous active period in the first half of 2009 analyzed in detail by Marscher et al. (2010), Abdo et al. (2010a), and D'Ammando et al. (2011), and they partially overlap with the optical/NIR data from SMARTS analyzed by Bonning et al. (2012) and Chatterjee et al. (2012). In 2009, a series of gamma-ray flares was accompanied by prominent optical/NIR activity, in contrast to the situation observed in 2011.

The long-term SMARTS data indicate the existence of a lower limit to the optical flux at the level of $F_{\rm min} \simeq 3 \times 10^{-12}$ erg s^{-1} cm^{-2} (see also Marscher et al. 2010). In the J and R bands (but also in V and B), this flux level was significantly

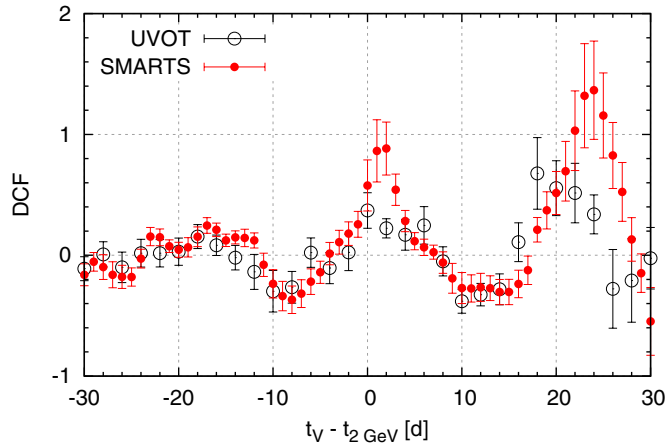

Figure 4. Discrete correlation function (DCF; Edelson & Krolik 1988) calculated between the *Fermi*/LAT light curve at 2 GeV and the optical light curves in the V band using either SMARTS ($\Delta t = 1$ day) or *Swift*/UVOT ($\Delta t = 2$ days) data (see Figure 3). Positive argument values indicate optical signal delayed with respect to the gamma-ray signal.

(A color version of this figure is available in the online journal.)

exceeded only in the 2009 active state. The long-term constancy of the optical flux in quiet states indicates that it is not associated with the relativistic jet, but rather it is dominated by the thermal emission of the accretion disk. On the other hand, in the 2009 flaring state, the optical flux is most likely associated with jet synchrotron emission. The lack of correlated optical activity corresponding to the gamma-ray flares in the summer of 2011 can be explained by a low level of the synchrotron component in the optical/NIR band. We will use these clues in our attempt to model the broadband SED.

The long-term light-curve in the K band shows a somewhat distinct behavior from the J band and higher frequencies. The K flux approaches $F_{\rm min}$ only in early 2011, and shows stronger and faster variability in the quiet state. In Figure 7, we present a color–luminosity diagram based on the whole SMARTS data set for PKS 1510−089. We find that, while the $B-J$, $V-J$, and $R-J$ colors have a clear trend of being "redder-when-brighter," the $K-J$ color shows no such behavior. The $K-J$ part of the νF_ν SED is consistently soft, while the $J-B$ part is soft at high luminosities and hard at low luminosities. It appears that in the quiet state the K luminosity is rather poorly correlated with other SMARTS bands. All the above evidence suggests that the K band marks the high-energy cutoff/break of the synchrotron component.

4. MODELING THE BROADBAND SED

In this section, we attempt to model the broadband SED of PKS 1510−089 during our second *Herschel* epoch (H2), as presented in Figure 5. We employ the leptonic radiative code `Blazar` (Moderski et al. 2003), which incorporates the exact treatment of the inverse-Compton emission in the Klein–Nishina regime, synchrotron self-absorption, and pair-production absorption. `Blazar` calculates the evolution of electrons injected at a constant rate over a distance range between $r_0/2$ and r_0 into a relativistically propagating spherical shell. The resulting non-thermal radiation is integrated over the same scale, and effectively it is dominated by the contribution from r_0. The variability properties of the source, with gamma-ray flares having no

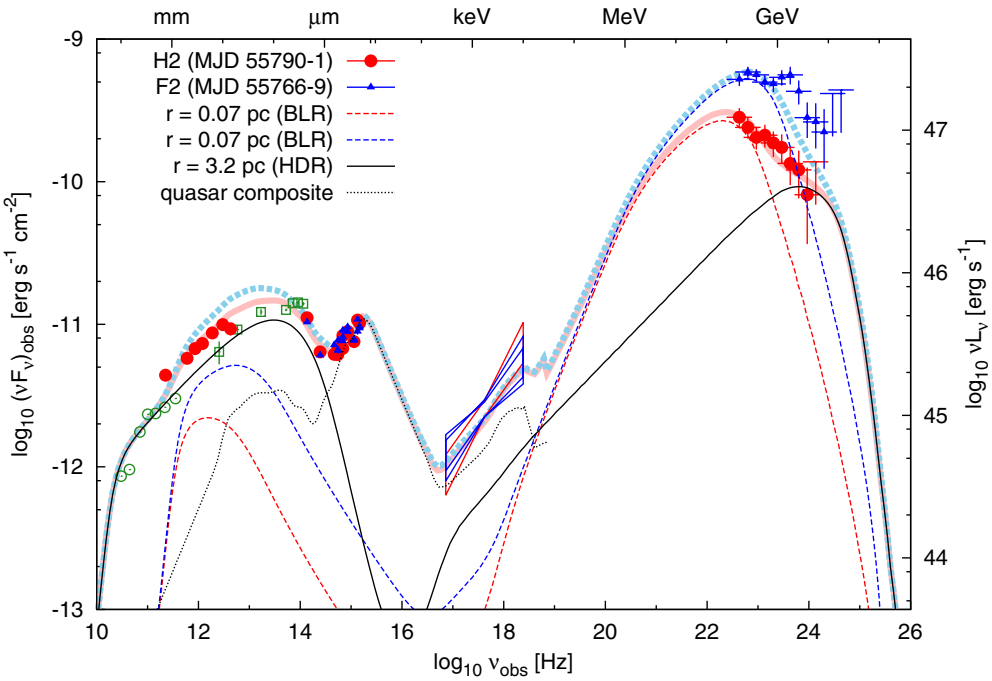

Figure 5. Broadband spectral energy distribution of PKS 1510−089 extracted for the second *Herschel* epoch (H2; red filled circles) and for the second gamma-ray flare (F2; blue triangles). The SMARTS and *Swift*/UVOT data are corrected for extinction, using values from Table 5. The green open circles show the *Planck* spectrum registered in 2010 February (*Planck* Collaboration et al. 2011), and the green open squares show the *Spitzer* spectrum registered in 2007 August–September (Malmrose et al. 2011). We also plot our SED model for the H2 state (thick solid light-red ribbon) and for the F2 state (thick dashed light-blue ribbon). Their three components are a slowly variable component produced beyond the edge of the dusty torus (solid lines; synchrotron radiation for $\nu_{\rm obs,16} < 1$; EC(HDR) radiation otherwise; negligible contribution from SSC and EC(BLR)), a rapidly variable component produced in the broad-line region (dashed lines—red for H2; blue for F2; synchrotron radiation for $\nu_{\rm obs,16} \lesssim 1$; EC(BLR) otherwise; marginal contribution from SSC at $\nu_{\rm obs,17} \sim 1$ for F2; negligible contribution from EC(HDR)), and a composite spectrum of radio-loud quasars (Elvis et al. 1994; dotted line).

(A color version of this figure is available in the online journal.)

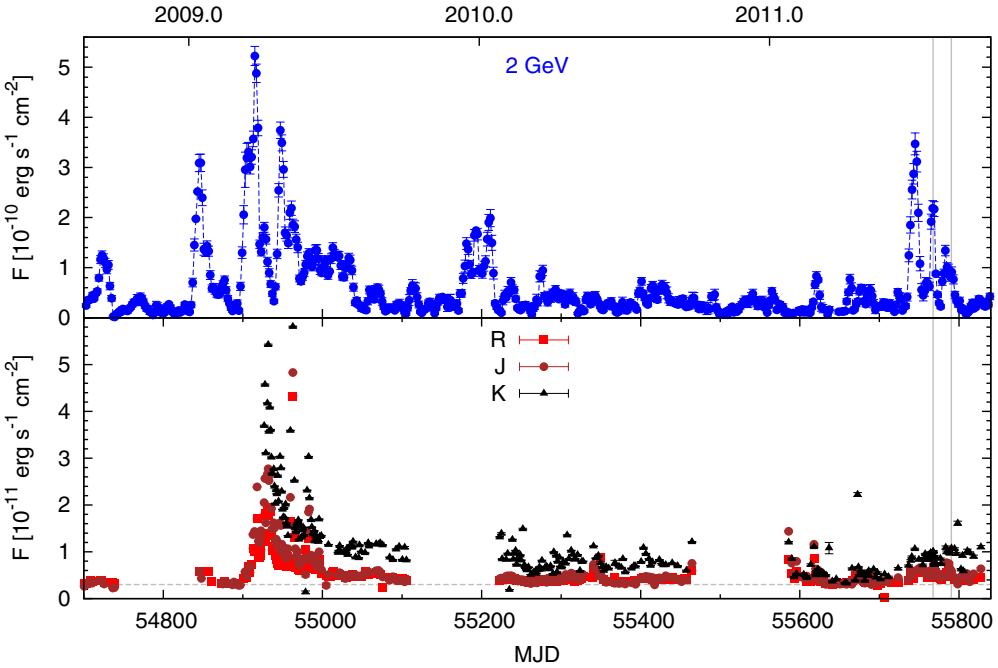

Figure 6. Long-term light curves of PKS 1510−089. The top panel shows the *Fermi*/LAT flux modeled in six-day time intervals by fitting a power law in the energy range between 200 MeV and 300 GeV, and taking the νF_ν value corresponding to 2 GeV. The bottom panel shows the optical/NIR data from SMARTS. The vertical lines mark epochs F2 and H2, for which the broadband SEDs were extracted.

(A color version of this figure is available in the online journal.)

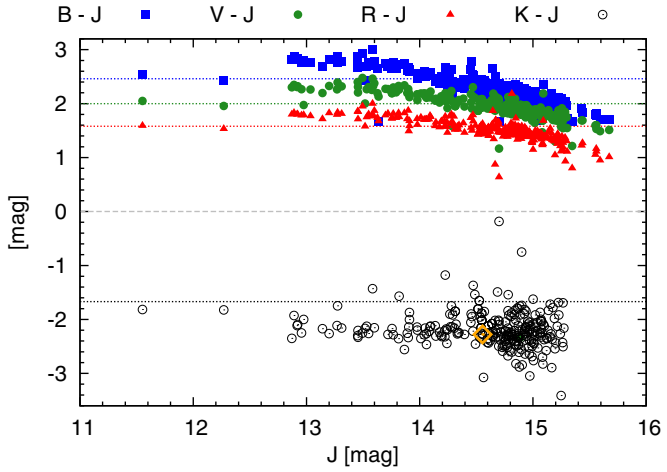

Figure 7. Optical/NIR colors of PKS 1510−089 plotted against the J magnitude based on the long-term SMARTS data. The dotted lines mark the color values corresponding to a flat SED (νF_ν). The orange point marks the $K-J$ color corresponding to the second *Herschel* epoch (H2; MJD 55790).

(A color version of this figure is available in the online journal.)

corresponding activity in the optical and IR bands, indicate that more than one emitting region is present. However, we begin by considering a one-zone model and a formal discussion of the physical constraints imposed by it.

In the optical/UV band, the hard spectrum, the lack of long-term flux variations, and the presence of a lower limit on the observed flux favor the dominance of a thermal component. In Figure 5, we plot the composite spectrum for radio-loud quasars from Elvis et al. (1994), normalizing it to the observed UV flux. We note that the composite spectrum nicely matches the observed optical/UV spectral index of PKS 1510−089, and it is also in reasonable agreement with the simultaneous X-ray spectrum. Although the observed X-ray flux is higher than the normalized composite spectrum by a factor ∼1.6, taking into account all the uncertainties and caveats involved in calculating the composite spectrum—in particular the observed scatter of the UV/X-ray luminosity ratio in quasars—we consider this discrepancy to be marginal. Therefore, at least a partial contribution of the hot accretion disk corona to the observed X-ray emission is likely, and this can explain the relatively low variability amplitude observed in PKS 1510−089 in the X-ray band over several years (Marscher et al. 2010).

The bolometric luminosity of the accretion disk is estimated by integrating the normalized spectrum of the quasar composite, excluding its infrared and X-ray components, which yields $L_{\rm d} \simeq 5 \times 10^{45}$ erg s^{-1}. Using this value, we can estimate the characteristic radii of the broad-line region (BLR), $r_{\rm BLR} \simeq 0.07$ pc, and the hot-dust region (HDR), $r_{\rm HDR} \simeq 2.9$ pc $\times\, T_3^{-2.6}$ (see Tavecchio & Ghisellini 2008; Nenkova et al. 2008; Sikora et al. 2009). Within these radii, the energy density of external radiation fields is roughly independent of the radius, and in the external frame is given by $u_{\rm ext} \simeq \xi_{\rm ext} L_{\rm d}/(4\pi c r_{\rm ext}^2)$, where $\xi_{\rm ext}$ is the covering factor of the medium reprocessing the accretion disk radiation, and "ext" stands either for "BLR" or "HDR."

As we argued in the previous section, the broadband SED up to the K band can be explained by a single synchrotron component. However, the GeV gamma-ray emission is most likely due to the Comptonization of external radiation (external-Compton, EC). Let us assume for a moment that these components are produced by the same population of ultra-relativistic electrons. This imposes two direct observational constraints. First, the luminosity ratio of the EC component to the synchrotron component, or the Compton dominance parameter, is $q = L_{\rm EC}/L_{\rm syn} \simeq 55$. Second, the frequency ratio of the peaks of the two components is $w = \nu_{\rm EC}/\nu_{\rm syn} \simeq 4.3 \times 10^8$. Sikora et al. (2009) showed that there is a direct relation between these two parameters that depends only on the covering factor $\xi_{\rm ext}$ and the energy of external

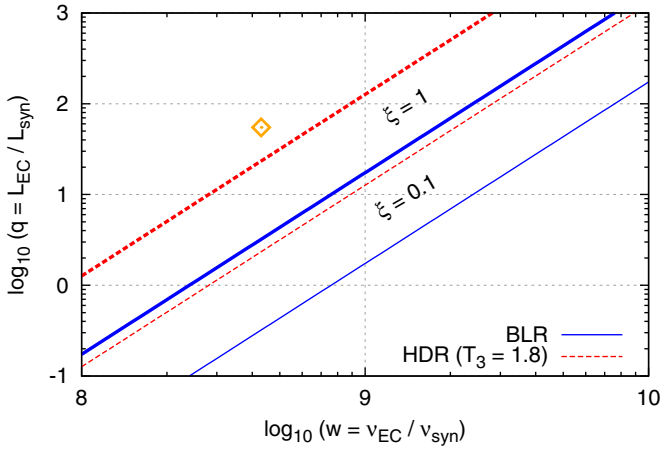

Figure 8. Parameter space of the peak frequency ratio $w = \nu_{\rm EC}/\nu_{\rm syn}$ of the external-Compton to synchrotron components produced by electrons of the same energy, and the Compton dominance parameter $q = L_{\rm EC}/L_{\rm syn}$. For a given energy of external photons and a covering factor ξ of the external radiation source, q is a function of w. Solid lines: constraints for the broad-line region; dashed lines: constraints for the hot-dust region; thin lines: $\xi = 0.1$; thick lines: $\xi = 1$. The orange point marks the location for PKS 1510−089 during the second *Herschel* epoch (H2; MJD 55790).

(A color version of this figure is available in the online journal.)

photons in the external frame (see their Equation (52)). It can be expressed as

$$\xi_{\rm BLR} \simeq 0.6 \times \frac{q_1}{w_9^2}\,, \quad \xi_{\rm HDR} \simeq 1.7 \times \frac{q_1}{w_9^2 T_3^{5.2}}\,, \qquad (4)$$

where T is the dust temperature.[18] These relations are shown in Figure 8, adopting $T_3 = 1.8$. Typically assumed values of the covering factor are $\xi_{\rm ext} \sim 0.1$–0.3. The observed values of q and w for PKS 1510−089 in the H2 state require $\xi_{\rm ext} \gg 1$, which is physically forbidden. Similar constraints on q and w also allow us to rule out the synchrotron-self-Compton (SSC) mechanism as the origin of the gamma-ray emission. Hence, *it is not possible to fit the infrared and gamma-ray parts of the SED with a single-zone model.*

The observed synchrotron and EC components must be produced at distinct locations in the jet, where the local values of q are different. Since the EC process proceeds in the Thomson regime, we have $q \simeq u'_{\rm ext}/u'_{\rm B}$, where $u'_{\rm B} = B'^2/(8\pi)$ is the magnetic energy density in the jet co-moving frame. We assume that the magnetic field scales as $B' \propto 1/r$, while the external radiation fields in the co-moving frame are approximated with $u'_{\rm ext}(r) \simeq (4/3)\Gamma_{\rm j}^2 u_{\rm ext}/[1 + (r/r_{\rm ext})^{\beta_{\rm ext}}]$, where $\Gamma_{\rm j}$ is the jet Lorentz factor, and we choose $\beta_{\rm BLR} = 3$ and $\beta_{\rm HDR} = 4$ (see also Hayashida et al. 2012). We further assume that the observed gamma-ray emission is produced in the BLR—this is supported by the variability timescale of the order of days observed exclusively in the gamma-ray band. We model this component at $r_0 = r_{\rm BLR}$, adopting $\Gamma_{\rm j} = 20$, a half-opening angle $\theta_{\rm j} = 1/\Gamma_{\rm j}$, and the covering factors $\xi_{\rm BLR} = \xi_{\rm HDR} = 0.1$. The high Compton dominance is assured by taking a relatively weak magnetic field $B' = 1\ {\rm G} \times (r_{\rm BLR}/r)$. We inject electrons with a broken power-law distribution of the random Lorentz factors, $N_\gamma \propto \gamma^{-p_{\rm i}}$, with $p_1 = 1.1$ for $\gamma < \gamma_{\rm br}$, and $p_2 = 4$ for $\gamma > \gamma_{\rm br}$. A very hard low-energy slope is necessary to avoid the EC component contributing to the observed X-ray emission. The injected electron energy distribution is softened by $\Delta p = 1$ due to efficient cooling above a cooling break located at $\gamma_{\rm c} \simeq 15$. Our choice of $\gamma_{\rm br} = 270$ places the EC peak in the low-energy end of the *Fermi*/LAT range (∼100 MeV), and the synchrotron peak in the middle of the *Herschel* range (∼250 μm). Parameters of this model are listed in Table 7.

[18] These relations are valid as long as the EC process proceeds in the Thomson regime. The observed energy of EC radiation produced in the Thomson regime is $E_{\rm EC,obs} < (m_{\rm e}c^2)^2/[12(1+z)E_{\rm ext}] = 16\ {\rm GeV}/(E_{\rm ext}/1\ {\rm eV})$, where $E_{\rm ext}$ is the energy of external radiation in the external frame (Ackermann et al. 2010). Even in the more constraining case of BLR with $E_{\rm ext} = 10$ eV, we find that $E_{\rm EC,obs} < 1.6$ GeV, which is satisfied in PKS 1510−089 by the observationally constrained spectral peak of the high-energy component.

Table 7
Parameters of SED Models Shown in Figure 5

	H2 (BLR)	F2 (BLR)	H2 (HDR)
r_0 (pc)	0.07	0.07	3.2
$\Gamma_{\rm j}$	20	20	20
$B'(r)$ (G)	1	1	0.022
p_1	1.1	1.1	2.2
p_2	4	4	6
$\gamma_{\rm min}$	1	1	1
$\gamma_{\rm br}$	270	500	10^4
$\gamma_{\rm max}$	2×10^4	2×10^4	3×10^5
$K_{\rm e}$ ($\rm s^{-1}$)	3×10^{46}	3×10^{46}	3×10^{49}

The observed infrared emission must be produced in a region of low Compton dominance. Such a region cannot be found, at least for our parameter choice, between $r_{\rm BLR}$ and $r_{\rm HDR}$. Hence, we model this emission at $r_0 = 10^{19}$ cm $\simeq 5\,r_{\rm HDR}$. The injected electron energy distribution is a broken power law with $p_1 = 2.2$, $p_2 = 6$, and $\gamma_{\rm br} = 10^4$. The low-energy slope p_1 is chosen to match the *Herschel* spectrum. The cooling is inefficient, and thus no cooling break is present. The EC component extends just below the observed X-ray emission and the gamma-ray emission in the 1–10 GeV range. On the low-energy end of the SED, we find the synchrotron emission to be self-absorbed below the frequency $\nu_{\rm abs} \sim 40$ GHz. This value is characteristic for the distance scale of a few parsec (Sikora et al. 2008), however, it is twice lower than the frequency of the spectral break detected by *Planck* in 2010 February (*Planck* Collaboration et al. 2011). The synchrotron self-absorption threshold frequency can be increased by allowing the jet to be more collimated, e.g., due to the formation of reconfinement shocks (Komissarov & Falle 1997; Nalewajko & Sikora 2009; Bromberg & Levinson 2009).

With a model of the H2 (low) spectral state on hand, we attempted to model a transition to the F2 (high) state. In Figure 5, we show a model of the F2 state obtained by varying a single parameter of the H2 state model, the break energy of the injected electron distribution of the SED component produced in the BLR (see also Anderhub et al. 2009), $\gamma_{\rm br} = 500$ (instead of $\gamma_{\rm br} = 270$). This resulted in a substantial increase of the gamma-ray flux and a modest increase of the IR flux, satisfying the observational constraint that the NIR, optical/UV, and X-ray fluxes remain roughly constant. This scenario predicts a correlated variability between MIR and gamma-ray bands, i.e., that the F2 gamma-ray flare had a weak MIR counterpart. Unfortunately, we do not have simultaneous MIR data to verify this prediction. This simple model also underpredicts the gamma-ray flux at 1–2 GeV, and thus an additional spectral component may be required in this energy range. While other scenarios of a spectral transition between H2 and F2 are certainly possible, this seems to be the only solution involving a change of a single parameter.

5. DISCUSSION

The FIR spectrum of PKS 1510−089 measured by *Herschel* is consistent with a simple power-law model. We did not find any direct evidence for a double synchrotron component, like the sharp spectral features observed by Ogle et al. (2011) in 3C 454.3 and Hayashida et al. (2012) in 3C 279. However, indirect evidence suggests the existence of a second synchrotron component of much lower luminosity. We showed that it is not possible to fit the entire SED of PKS 1510−089 with a one-zone synchrotron-EC model, because the observed Compton dominance $q = L_{\rm EC}/L_{\rm SYN}$ is not compatible with the relative position of the synchrotron and EC peaks. The SED can be explained by a model consisting of two blazar zones characterized by different values of q, and thus spatially separated. In addition, the optical/UV spectrum suggests the presence of a thermal component, presumably produced in the accretion disk, with a further implication that the associated accretion disk corona can at least partly explain the X-ray emission.

This model is very tightly constrained by the observational data, and thus has several testable predictions. The thermal quasar emission is expected to be variable over very long timescales (months/years), the component produced in the HDR should vary over weeks, and the component produced in the BLR over days. In our model, we should expect such variability timescales in the optical/UV, infrared, and gamma-ray bands, respectively. This is roughly consistent with the 2011 data for PKS 1510−089 presented in Figure 3 and the long-term data shown in Figure 6. The fast optical flares observed in 2009 were significantly brighter and strongly polarized, and thus require a contribution of a synchrotron spectral component in the optical band. Such a component could extend to the FIR range, depending on the synchrotron self-absorption threshold. For a compact emitting region, typical for its location in the BLR, self-absorption could begin in the FIR range, producing a noticeable spectral break (Hayashida et al. 2012). For a large emitting region, typical for its location in the HDR, the self-absorption begins in the (sub)millimeter range (Sikora et al. 2008). Thus, in high gamma-ray/optical states, like the one observed in 2009, we expect two clear signatures in the FIR band of the synchrotron component produced in a compact region: a sharp spectral break and variability on daily timescales. Further FIR observations of this or other luminous blazars are necessary to test these predictions.

Our model is different from that of Abdo et al. (2010a), who analyzed the 2009 active state of PKS 1510−089. We first note that they adopted different electron energy distributions: with $p \simeq 3.2$ and $\gamma_{\rm max} = 2.2 \times 10^4$, their synchrotron components were relatively high and soft, extending into the far-UV band (they adopted $B' = 1$ G and $\Gamma_{\rm j} \simeq 15$). Unbeknownst to these authors, their synchrotron models are rather consistent with our *Herschel* data, at least in the 2009 March state, thanks to the introduction of a break in the electron energy distribution at $\gamma_{\rm br} \simeq 200$. However, these models are not consistent with very soft NIR spectra that we identify in the SMARTS data, and that, to a lesser degree, can be seen in Figure 24 of Abdo et al. (2010a). As we show in Figure 7, the $K-J$ color in the H2 epoch is quite typical for this source.

To explain the 2009 flaring state, when the optical/NIR flux was well correlated with the gamma-ray flux, in our two-zone model, one of the synchrotron components should dominate the thermal accretion disk emission. The fast variability of the 2009 flares indicates that it should be the component produced at a shorter distance scale within the jet, i.e., the one located in the BLR (Tavecchio et al. 2010). Now, we know that the value of Compton dominance varied in the range of $q \sim 10$–50. Our BLR component has a very large $q \simeq 200$ due to a rather low local magnetic field strength. Hence, the 2009 activity could have been accompanied by a significant increase of the magnetic field, which can be achieved via compression by a strong shock wave. Indeed, Marscher et al. (2010) report a superluminal knot observed with VLBA at 7 mm, the emergence of which (passage through the 7 mm radio core) roughly coincided with the main gamma-ray/optical flare. Also during that flare, a strong increase in the optical polarization degree was observed (see also Sasada et al. 2011), which is consistent with a strong shock wave compressing the magnetic fields. Hence, the 2009 activity of PKS 1510−089 was most likely caused by additional dissipation provided by a passing shock wave, and apparently in the summer of 2011 such an additional factor was not present.

Kataoka et al. (2008) and Abdo et al. (2010b) observed PKS 1510−089 in 2006 and 2009 with the *Suzaku* X-ray telescope and various other facilities. The focus of their work was on the soft X-ray part of the SED, but they also measured a hard optical/UV spectrum, which they interpreted as thermal emission from the accretion disk. They adopted a soft synchrotron component peaking in the FIR range. Using non-simultaneous data, they noticed a very soft NIR spectrum and interpreted it as an excess resulting from the starlight of the host galaxy. The long-term SMARTS data invalidate this interpretation, because they show that the large-amplitude NIR variability is not associated with a correlated variability of the $K-J$ color. The strong variability amplitude in the NIR band can be explained only by the synchrotron emission. Moreover, a hard synchrotron component inferred from our *Herschel* observations is consistent with previous observations of PKS 1510−089 by the *Planck* and *Spitzer* satellites (*Planck* Collaboration et al. 2011; Malmrose et al. 2011; see Figure 5). A similar spectral shape of the synchrotron component in PKS 1510−089 was adopted by D'Ammando et al. (2009).

The possibility that the X-ray emission of PKS 1510−089 is produced at least partly in the accretion disk corona was considered neither by Kataoka et al. (2008) nor by Abdo et al. (2010b), even though the X-ray flux measured with *Suzaku* is comparable to that presented in this work. The long-term X-ray light curves of PKS 1510−089 presented by Marscher et al. (2010) indicate a flux lower limit of 5×10^{-12} erg s^{-1} cm^{-2} in the 2.4–10 keV range, which corresponds to 8×10^{-12} erg s^{-1} cm^{-2} in the 0.3–10 keV range for a photon index of $\Gamma_{\rm X} = 1.5$. Our estimate of the 0.3–10 keV X-ray flux attributed to the accretion disk corona is $\sim 6 \times 10^{-12}$ erg s^{-1} cm^{-2}, which is consistent with the lower limit given above. Another possible signature of the coronal emission contributing to the X-ray band is fluorescent Fe emission line. However, even the very deep *Suzaku* observations reported by Kataoka et al. (2008) do not reveal any hint of such lines, although, such lines are generally hard to detect even in intrinsically similar sources with misaligned jets (steep-spectrum radio quasars and broad-line radio galaxies; e.g. Grandi et al. 2006; Fukazawa et al. 2011). We also note that our *Swift*/XRT data are of insufficient quality to verify the presence of the soft X-ray excess detected by *Suzaku*.

Our inference of two separate energy dissipation regions ("blazar zones") in AGN jets is consistent with the works of Ogle et al. (2011) and Hayashida et al. (2012). If confirmed by further comprehensive studies of multiwavelength emission

of blazars, it has significant implications for the long-standing theoretical problem of the location of blazar zones and the underlying mechanisms of energy dissipation and particle acceleration. The answer to this puzzle may turn out to be quite complex. At the distance scale of ∼0.1 pc, in the BLR, possible dissipation mechanisms could be internal shocks, produced by collisions of jet portions of high Lorentz factor contrast (Sikora et al. 1994; Spada et al. 2001; Tavecchio et al. 2010), or magnetic reconnection enabled by global magnetic field reversals (Nalewajko et al. 2011) or current-driven instabilities (Giannios & Spruit 2006; Nalewajko & Begelman 2012). At the distance scale of 3 pc, in the HDR, dissipation could proceed via reconfinement shocks, produced by interaction of the jet with the external medium (Daly & Marscher 1988; Sikora et al. 2008; Nalewajko 2012), and possibly driving turbulence (Marscher 2012). The need for distinct particle acceleration mechanisms is underlined by the different energy distributions of injected electrons required to explain the observational data. A hard low-energy electron index for the component produced in the BLR, $p_1 = 1.1$, suggests magnetic reconnection (e.g., Zenitani & Hoshino 2001; Lyubarsky & Liverts 2008), while the one for the component produced in the HDR, $p_1 = 2.2$, constrained directly by the *Herschel* data, may favor the shock acceleration (e.g., Bednarz & Ostrowski 1998). Thus, a possible scenario for the overall activity of PKS 1510−089 may involve dissipation via magnetic reconnection at sub-parsec scales and additional dissipation via recollimation shocks at supra-parsec scales. Strong breaks in the injected electron energy distributions, with $p_2 - p_1 \simeq 3$–4, may indicate the variation of $\gamma_{\rm max}$ along the propagation of the emitting region. That $\gamma_{\rm br}$ is much larger in the HDR models than in the BLR models is consistent with less efficient cooling and/or longer source evolution timescale in the HDR. However, a definite theory of particle acceleration in relativistic sources is necessary to explain the observed spectral breaks.

6. CONCLUSIONS

We observed blazar PKS 1510−089 with the *Herschel Space Observatory*, using its PACS and SPIRE photometric instruments. We detected the source consistently with all six filters at five epochs in the relatively quiet state from 2011 mid-July to early September. We did not find a significant variability amplitude in the FIR range. The FIR SED for each epoch is consistent with a power-law model, with a slight harder-when-brighter trend.

We collected simultaneous multiwavelength data from *Fermi*/LAT, *Swift*, SMARTS, and SMA, to place our *Herschel* observations within a broader context. Analysis of the short-term multiwavelength light curves indicates a low fractional variability in all bands between the millimeter and X-ray, accompanied by two gamma-ray flares directly preceding the *Herschel* observations. Broadband SEDs were extracted for two epochs—the second *Herschel* epoch ("H2") and the second gamma-ray flare ("F2"). They show different gamma-ray spectra, with the flaring state spectrum being harder and more complex than the quiet state spectrum. They also show a consistent spectral structure in the NIR/optical/UV range—a very soft NIR ($K - J$) spectrum and a hard optical/UV spectrum. We also compare the long-term gamma-ray and optical/NIR activities, using the *Fermi*/LAT and SMARTS data. The SMARTS data reveal the existence of a lower limit on flux in the J and R filters, and a noticeably different behavior of the K flux. The $K - J$ color does not depend on the J luminosity, in contrast to the "optical-J" colors, which show the typical "redder-when-brighter" trends.

We interpret the optical/UV spectrum in terms of thermal emission from the accretion disk. This is supported by the hard spectrum and the existence of the lower limit to the flux. The associated accretion disk corona can partly explain the X-ray spectrum. The soft NIR spectrum is interpreted as the high-energy cutoff in a synchrotron component. This component cannot be produced in the same region as the main gamma-ray emission for two reasons: (1) their variations are not correlated, (2) in the synchrotron-EC scenario using a single population of electrons, the relation between the Compton dominance parameter $q = L_{\rm EC}/L_{\rm syn} \simeq u'_{\rm ext}/u'_{\rm B}$ and the emitted frequency ratio $w = \nu_{\rm EC}/\nu_{\rm syn}$ is strongly constrained. A one-zone leptonic model would require an unrealistically high energy density of the external radiation to match the NIR and gamma-ray spectra simultaneously. We consider a two-zone model, with the infrared emission produced in the jet region of a small q and the gamma-ray emission produced in the region of a very large q. We find a consistent model, in which the high-q region is associated with the BLR, and the low-q region is located in the HDR. We show that "orphan" gamma-ray flares can be explained by varying solely the break energy of the electron energy distribution injected in the high-q (BLR) region. Hence, we identify the *Herschel* results mainly with the synchrotron emission produced at the supra-parsec scale, and the two gamma-ray flares with the EC (BLR) component produced at the sub-parsec scale.

We acknowledge financial support by the Polish NCN grant DEC-2011/01/B/ST9/04845, the NSF grant AST-0907872, the NASA ATP grant NNX09AG02G, the NASA Fermi GI grant NNX11AO39G, the NASA JPL/IPAC Herschel GO grant RSA 1433865 to Stanford University, and a DoE support to SLAC via contract DE-AE3-76SF00515. We acknowledge support from the Faculty of European Space Astronomy Center (ESAC).

Herschel is an ESA space observatory with science instruments provided by European-led Principal Investigator consortia and with important participation from NASA.

The *Fermi*-LAT Collaboration acknowledges generous ongoing support from a number of agencies and institutes that have supported both the development and the operation of the LAT as well as scientific data analysis. These include the National Aeronautics and Space Administration and the Department of Energy in the United States, the Commissariat à l'Energie Atomique and the Centre National de la Recherche Scientifique/Institut National de Physique Nucléaire et de Physique des Particules in France, the Agenzia Spaziale Italiana and the Istituto Nazionale di Fisica Nucleare in Italy, the Ministry of Education, Culture, Sports, Science and Technology (MEXT), High Energy Accelerator Research Organization (KEK) and Japan Aerospace Exploration Agency (JAXA) in Japan, and the K. A. Wallenberg Foundation, the Swedish Research Council and the Swedish National Space Board in Sweden. Additional support for science analysis during the operations phase is gratefully acknowledged from the Istituto Nazionale di Astrofisica in Italy and the Centre National d'Études Spatiales in France.

We acknowledge the use of NASA's *Swift* Observatory.

The Submillimeter Array (SMA) is a joint project between the Smithsonian Astrophysical Observatory and the Academia Sinica Institute of Astronomy and Astrophysics and is funded by the Smithsonian Institution and the Academia Sinica.

REFERENCES

Abdo, A. A., Ackermann, M., Agudo, I., et al. 2010a, ApJ, 721, 1425
Abdo, A. A., Ackermann, M., Ajello, M., et al. 2010b, ApJ, 716, 835
Abdo, A. A., Ackermann, M., Ajello, M., et al. 2010c, ApJS, 188, 405
Ackermann, M., Ajello, M., Baldini, L., et al. 2010, ApJ, 721, 1383
Anderhub, H., Antonelli, L. A., Antoranz, P., et al. 2009, ApJ, 705, 1624
Atwood, W. B., Abdo, A. A., Ackermann, M., et al. 2009, ApJ, 697, 1071
Bednarz, J., & Ostrowski, M. 1998, Phys. Rev. Lett., 80, 3911
Bessell, M. S., Castelli, F., & Plez, B. 1998, A&A, 333, 231
Bonning, E., Urry, C. M., Bailyn, C., et al. 2012, ApJ, 756, 13
Bromberg, O., & Levinson, A. 2009, ApJ, 699, 1274
Cardelli, J. A., Clayton, G. C., & Mathis, J. S. 1989, ApJ, 345, 245
Chatterjee, R., Bailyn, C. D., Bonning, E. W., et al. 2012, ApJ, 749, 191
Clegg, P. E., Gear, W. K., Ade, P. A. R., et al. 1983, ApJ, 273, 58
D'Ammando, F., & Gasparrini, D. 2011, ATel, 3473
D'Ammando, F., Pucella, G., Raiteri, C. M., et al. 2009, A&A, 508, 181
D'Ammando, F., Raiteri, C. M., Villata, M., et al. 2011, A&A, 529, A145
Daly, R. A., & Marscher, A. P. 1988, ApJ, 334, 539
Edelson, R. A., & Krolik, J. H. 1988, ApJ, 333, 646
Elvis, M., Wilkes, B. J., McDowell, J. C., et al. 1994, ApJS, 95, 1
Fermi-LAT Collaboration. 2012, ApJS, 203, 4
Fukazawa, Y., Hiragi, K., Mizuno, M., et al. 2011, ApJ, 727, 19
Gasparrini, D., & Cutini, S. 2011, ATel, 3579
Giannios, D., & Spruit, H. C. 2006, A&A, 450, 887
Grandi, P., Malaguti, G., & Fiocchi, M. 2006, ApJ, 642, 113
Griffin, M. J., Abergel, A., Abreu, A., et al. 2010, A&A, 518, L3
Gurwell, M. A., Peck, A. B., Hostler, S. R., Darrah, M. R., & Katz, C. A. 2007, in ASP Conf. Ser. 375, From Z-Machines to ALMA: (Sub)Millimeter Spectroscopy of Galaxies, ed. A. J. Baker et al. (San Francisco, CA: ASP), 234
Haas, M., Chini, R., Meisenheimer, K., et al. 1998, ApJ, 503, L109
Hauser, M., Lenain, J. P., Wagner, S., & Hagen, H. 2011, ATel, 3509
Hayashida, M., Madejski, G. M., Nalewajko, K., et al. 2012, ApJ, 754, 114
Impey, C. D., & Neugebauer, G. 1988, AJ, 95, 307
Kataoka, J., Madejski, G., Sikora, M., et al. 2008, ApJ, 672, 787
Komissarov, S. S., & Falle, S. A. E. G. 1997, MNRAS, 288, 833
Lyubarsky, Y., & Liverts, M. 2008, ApJ, 682, 1436
Malmrose, M. P., Marscher, A. P., Jorstad, S. G., Nikutta, R., & Elitzur, M. 2011, ApJ, 732, 116
Marscher, A. P. 2012, arXiv:1201.5402
Marscher, A. P., Jorstad, S. G., Larionov, V. M., et al. 2010, ApJ, 710, L126
Mattox, J. R., Bertsch, D. L., Chiang, J., et al. 1996, ApJ, 461, 396
Moderski, R., Sikora, M., & Błażejowski, M. 2003, A&A, 406, 855
Nalewajko, K. 2012, MNRAS, 420, L48
Nalewajko, K., & Begelman, M. C. 2012, MNRAS, in press (arXiv:1208.0007)
Nalewajko, K., Giannios, D., Begelman, M. C., Uzdensky, D. A., & Sikora, M. 2011, MNRAS, 413, 333
Nalewajko, K., & Sikora, M. 2009, MNRAS, 392, 1205
Nenkova, M., Sirocky, M. M., Nikutta, R., Ivezić, Ž., & Elitzur, M. 2008, ApJ, 685, 160
Nolan, P. L., Abdo, A. A., Ackermann, M., et al. 2012, ApJS, 199, 31
Pilbratt, G. L., Riedinger, J. R., Passvogel, T., et al. 2010, A&A, 518, L1
Planck Collaboration, Aatrokoski, J., Ade, P. A. R., et al. 2011, A&A, 536, A15
Poglitsch, A., Waelkens, C., Geis, N., et al. 2010, A&A, 518, L2
Poole, T. S., Breeveld, A. A., Page, M. J., et al. 2008, MNRAS, 383, 627
Ogle, P. M., Wehrle, A. E., Balonek, T., & Gurwell, M. A. 2011, ApJS, 195, 19
Orienti, M., Koyama, S., D'Ammando, F., et al. 2012, arXiv:1210.4319
Ott, S. 2010, in ASP Conf. Ser. 434, Astronomical Data Analysis Software and Systems XIX, ed. Y. Mizumoto, K.-I. Morita, & M. Ohishi (San Francisco, CA: ASP), 139
Sasada, M., Uemura, M., Fukazawa, Y., et al. 2011, PASJ, 63, 489
Sikora, M., Begelman, M. C., & Rees, M. J. 1994, ApJ, 421, 153
Sikora, M., Moderski, R., & Madejski, G. M. 2008, ApJ, 675, 71
Sikora, M., Stawarz, Ł., Moderski, R., Nalewajko, K., & Madejski, G. M. 2009, ApJ, 704, 38
Spada, M., Ghisellini, G., Lazzati, D., & Celotti, A. 2001, MNRAS, 325, 1559
Tavecchio, F., & Ghisellini, G. 2008, MNRAS, 386, 945
Tavecchio, F., Ghisellini, G., Bonnoli, G., & Ghirlanda, G. 2010, MNRAS, 405, L94
Wagner, S., & Behera, B. 2010, HEAD Meeting, 11, 27.06
Zenitani, S., & Hoshino, M. 2001, ApJ, 562, L63